The Astronomical Journal, 169:163 (10pp), 2025 March https://doi.org/10.3847/1538-3881/adadf9

JWST 1.5 μm and 4.8 μm Photometry of Y Dwarfs

Loïc Albert[1,21], Sandy K. Leggett[2,21], Per Calissendorff[3], Thomas Vandal[1], J. Davy Kirkpatrick[4], Daniella C. Bardalez Gagliuffi[5,6], Matthew De Furio[7], Michael Meyer[3], Charles A. Beichman[8], Adam J. Burgasser[9], Michael C. Cushing[10], Jacqueline Kelly Faherty[11], Clémence Fontanive[1], Christopher R. Gelino[4], John E. Gizis[12], Alexandra Z. Greenbaum[13], Frantz Martinache[14], Mamadou N'Diaye[14], Benjamin J. S. Pope[15,16], Thomas L. Roellig[17], Johannes Sahlmann[18], Anand Sivaramakrishnan[11,19,20], and Marie Ygouf[8]

[1] Département de Physique, Observatoire du Mont-Mégantic and Institut Trottier de Recherche sur les exoplanètes, Université de Montréal,C.P. 6128, Succ. Centre-ville, Montréal, H3C 3J7, Québec, Canada; loic.albert@umontreal.ca
[2] NOIRLab - Gemini North, Hilo, HI 96720, USA
[3] Department of Astronomy, University of Michigan, Ann Arbor, MI 48109, USA
[4] California Institute of Technology, Pasadena, CA 91125, USA
[5] Department of Physics & Astronomy, Amherst College, 25 East Drive, Amherst, MA 01003, USA
[6] Department of Astrophysics, American Museum of Natural History,200 Central Park West, NY 10024, USA
[7] Department of Astronomy, University of Texas at Austin, Austin, TX 78712, USA
[8] Jet Propulsion Laboratory, California Institute of Technology, Pasadena, CA 91109, USA
[9] University of California, San Diego, La Jolla, CA 92093,USA
[10] Ritter Astrophysical Research Center, Department of Physics and Astronomy, University of Toledo, 2801 W. Bancroft Street, Toledo, OH 43606, USA
[11] Astrophysics Department,American Museum of Natural History, 79th Street at Central Park West, New York, NY 10024, USA
[12] Department of Physics and Astronomy, University of Delaware, Newark, DE 19716, USA
[13] IPAC, Mail Code 100-22, Caltech, 1200 E. California Blvd., Pasadena, CA 91125, USA
[14] Université Côte d'Azur, Observatoire de la Côte d'Azur, CNRS, Laboratoire Lagrange, France
[15] School of Mathematics and Physics, The University of Queensland, St Lucia,QLD 4072, Australia
[16] Centre for Astrophysics, University of Southern Queensland, West Street, Toowoomba, QLD 4350, Australia
[17] MS 245-6,NASA Ames Research Center, Moffett Field, CA 94035, USA
[18] European Space Agency (ESA), European Space Astronomy Centre (ESAC), Camino Bajo del Castillo s/n, 28692 Villanueva de la Cañada, Madrid, Spain
[19] Space Telescope Science Institute, 3700 San Martin Drive, Baltimore, MD 21218, USA
[20] Department of Physics and Astronomy, Johns Hopkins University, 3701 San Martin Drive, Baltimore, MD 21218, USA
Received 2024 December 10; revised 2025 January 21; accepted 2025 January 22; published 2025 February 24

Abstract

Brown dwarfs lack nuclear fusion and cool with time; the coldest known have an effective temperature below 500 K, and are known as Y dwarfs. We present a James Webb Space Telescope (JWST) photometric data set of Y dwarfs: 23 were imaged in wide-field mode, 20 using NIRCam with the F150W and F480M filters, and three using NIRISS with the F480M filter. We present an F480M versus F150W – F480M color–magnitude diagram for our sample, and other brown dwarfs with F150W and F480M colors synthesized from JWST spectra by S. A. Beiler et al. For one target, WISEA J083011.95+283716.0, its detection in the near-infrared confirms it as one of the reddest Y dwarfs known, with F150W – F480M = 9.62 mag. We provide its updated parallax and proper motion. One of the Beiler et al. Y dwarfs, CWISEP J104756.81+545741.6, is unusually blue, consistent with strong CO absorption seen in its spectrum, which the F480M filter is particularly sensitive to. The strong CO and the kinematics of the object suggest it may be very low mass and young. We update the resolved photometry for the close binary system WISE J033605.05–014350.4 AB, and find that the secondary is almost as cold as WISE 085510.83–071442.5, with $T_{\rm eff} \lesssim 300$ K, however the F150W – F480M color is significantly bluer, possibly suggesting the presence of water clouds. Astrometry is measured at the JWST epoch for the sample which is consistent with parallax and proper motion values reported by J. D. Kirkpatrick et al. and F. Marocco et al.

Unified Astronomy Thesaurus concepts: Brown dwarfs (185); Infrared photometry (792); Space astrometry (1541); Stellar atmospheres (1584)

1. Introduction

Y dwarfs are the coolest known class of brown dwarfs—objects with insufficient mass for sustained nuclear fusion at their core (A. Burrows et al. 2001). The Y dwarfs have effective temperatures ($T_{\rm eff}$) less than 500 K (J. D. Kirkpatrick et al. 2021); the coldest Y dwarf currently known, WISE 085510.83–071442.5, has $T_{\rm eff} \approx 260$ K (S. K. Leggett et al. 2021; K. L. Luhman et al. 2024; see also Section 5). Evolutionary models (M. S. Marley et al. 2021) calculate that field Y dwarfs, with ages of a few billion years (e.g., J. D. Kirkpatrick et al. 2021; W. M. J. Best et al. 2024), have masses of about 10 Jupiter masses ($M_{\rm Jup}$), within the planetary-mass regime, such that the properties of giant planets and cold brown dwarfs overlap significantly (C. V. Morley et al. 2014; A. P. Showman et al. 2019). Ultimately, establishing the nature of these low-mass objects, planets or brown dwarfs, needs to involve their formation pathways. To progress with that question requires a diversity of approaches: comparing and contrasting the properties of low-mass companions to host stars, e.g., orbital eccentricities (B. P. Bowler et al. 2020), exploring the lower mass limits of star formation

[21] These authors contributed equally to this work.

(J. D. Kirkpatrick et al. 2021, 2024), and characterizing the Y-dwarf multiplicity to understand their formation (C. Fontanive et al. 2023).

With our James Webb Space Telescope (JWST) Cycle 1 program (PID 2473, PI: Loïc Albert), we explore the multiplicity of 20 Y dwarfs with NIRCam kernel-phase interferometry (F. Martinache 2010; A. Ceau et al. 2019; J. Kammerer et al. 2023), using the F150W and F480M filters. In this paper, we report the photometric measurements for the sample, and also provide checks on the published proper motions and parallaxes of J. D. Kirkpatrick et al. (2021). A companion paper (T. Vandal et al. 2025, in preparation) presents the results of the search for companions for the entire sample. An early discovery of the first binary Y-dwarf system from this program was presented by P. Calissendorff et al. (2023). Another companion paper presents detailed modeling of the photometry of WISEA J083011.95+283716.0 (K. Matuszewska et al. 2025, in preparation). We supplement the photometry determined as part of PID 2473 with measurements of cold brown dwarfs using the F480M filter, executed as part of the Cycle 1 GTO programs 1189 (PI: Thomas L Roellig) and 1230 (PI: Catarina Alves de Oliveira).

Section 2 describes the sample and observations. Section 3 describes the data reduction and presents the photometric measurements. Section 4 discusses the kinematics of the sample. The brown dwarf colors are explored using color–magnitude diagrams and models in Section 5. Section 6 presents our conclusions.

2. Sample and Observations

2.1. Sample Selection

The target list of Y dwarfs was selected from the literature as available in 2020. We selected spectroscopically confirmed brown dwarfs as listed in J. D. Kirkpatrick et al. (2019, their Table 11) with $T_{\rm eff} < 500$ K within 15 pc of the Sun. For the NIRCam program (PID 2473), brown dwarfs calculated to be too close to known background objects during Cycle 1 were removed from the sample, as were known binary brown dwarfs. Two targets in that sample were observed for principal investigator Albert as part of GTO programs (PIDs 1189 and 1230) using NIRISS in imaging mode, which included two additional targets in the 15 pc Y-dwarfs sample (WISE J085510.83–071442.5 and WISEPA J182831.08+265037.8) as well as an additional point-spread function (PSF) calibration target, UGPS J072227.51–054031.2, a nearby T9 brown dwarf. The full sample is listed in Table 1 with discovery references, effective temperature values, parallax measurements, and CatWISE2020 W2 magnitudes. Hereafter, the targets will be written as WISE-hhmm, e.g., WISE-0855.

2.2. JWST NIRCam Imaging

NIRCam enables dual-band imaging in the blue ($\lambda \leqslant 2.4\ \mu$m) and red ($\lambda \geqslant 2.5\ \mu$m) channels simultaneously (M. J. Rieke et al. 2023). For the blue channel, we selected the F150W (1.5 μm) wide-band filter ($\Delta\lambda/\lambda = 10\%$) because most Y dwarfs had measurements in the ground-based *H*-band filter which is centered near 1.6 μm (see J. D. Kirkpatrick et al. 2019, 2021). For the red channel, we selected a filter at a wavelength where the Y dwarfs emit significant flux, the F480M (4.8 μm) medium-band filter ($\Delta\lambda/\lambda = 5\%$; C. V. Morley et al. 2014; A. C. Schneider et al. 2015).

We observed the sample in five groups of four targets, and specified that observations within a group were to be executed within 3 days. This strategy was designed to minimize any wave-front drift and, for each target, to be able to use the three other targets as PSF reference stars (assuming they were not binaries).

The integration times ranged, for a given target, between 30 minutes and 2.5 hr, which provided a signal-to-noise ratio (SNR) > 1000 in F480M. Achieving such a high SNR (or roughly 10^7 photons) at 4.8 μm was crucial to be able to use the kernel-phase interferometry analysis technique for our binary search. The SNRs in F150W were much lower (10–100) because of the extremely red $H - {\rm W2}$ colors of $\geqslant$6 magnitudes for this sample of Y dwarfs. Note that this high SNR is considered separately from the *absolute* flux calibration uncertainty for NIRCam, currently listed at 0.9% (F480M) and 0.4% (F150W) in the respective `photom` reference files found on the JWST Calibration Reference Data System (CRDS).[22]

Each target was observed over the 2.′2 × 2.′2 field of view of module B in FULL readout mode with dithered exposures. The first 12 targets used a five-point subpixel dither type (`SMALL-GRID-DITHER`) that was found to be suboptimal for bad pixel correction. It was switched to a larger (2.″9-8.″9) five-point primary dither strategy (`INTRAMODULEBOX`) enabling better bad pixel interpolation for the remaining eight targets. We attempted to center the target near pixels 1200, 700 on the long-wave detector (F480M band) corresponding to pixels near 400, 1400 in the short-wave detector NIRCB2 (F150W band) by using a target offset of $\Delta\alpha,\ \Delta\delta = +22.''0, -8.''0$. Errors in the position epoch entered in the Astronomer Proposal Tool caused significant deviations, in one case resulting in having the target off the F150W channel for two dithers. Table 2 lists the observations for targets observed as part of PID 2473.

2.3. JWST NIRISS Imaging

The target list was supplemented with three additional brown dwarfs, UGPS-0722, WISE-0855, and WISE-1828, observed with NIRISS in imaging mode using filters F480M + CLEARP to search for companions (see Table 2). One of the sources, UGPS-J0722, is a late T dwarf and not a Y dwarf, and is warmer than the rest of the sample, with $T_{\rm eff} \approx 540$ K (e.g., S. K. Leggett et al. 2021).

The WISE-0855 observation was accompanied by a contemporaneous calibrator star observation of UGPS-0722, intended to serve as a PSF reference for both WISE-0855 and WISE-1828. During the first epoch of observations of WISE-0855 and UGPS-0722 the Fine Guidance Sensor lost the guide-star lock and repeat observations of both targets were performed. A large SNR (>1000) was achieved for all three targets. Observations were undithered (staring) and centered on a bad-pixel-free region of the NIRISS detector. All observations with NIRISS were obtained in FULL subarray mode, except UGPS-0722, which was observed in SUB80 (80 × 80 pixels) to prevent saturation.

[22] https://jwst-crds.stsci.edu/

Table 1
Sample of Brown Dwarfs

Short Name	Full Name	Disk. Ref.	$T_{\rm eff}$ Est. K	$T_{\rm eff}$ Ref.	Parallax (mas)	W2 (mag)
NIRCam F150W+F480M Survey (Program ID 2473)						
WISE-0304	WISE J030449.03–270508.3	(1)	465 ± 88	(a)	73.1 ± 2.6	15.578 ± 0.041
WISE-0336AB	WISE J033605.05–014350.4AB	(2)	460 ± 79	(b)	99.8 ± 2.1	14.664 ± 0.023
WISE-0359	WISE J035934.06–540154.6	(2)	443^{+23}_{-19}	(c)	73.6 ± 2.0	15.412 ± 0.026
WISE-0410	WISEPA J041022.71+150248.5	(3)	451 ± 88	(a)	151.3 ± 2.0	14.104 ± 0.017
WISE-0535	WISE J053516.80–750024.9	(2)	496^{+28}_{-23}	(c)	68.7 ± 2.0	14.996 ± 0.020
WISE-0647	WISE J064723.23–623235.5	(4)	393 ± 88	(a)	99.5 ± 1.7	15.115 ± 0.018
WISE-0713	WISE J071322.55–291751.9	(2)	464 ± 88	(a)	109.3 ± 2.1	14.327 ± 0.016
WISE-0734	WISE J073444.02–715744.0	(2)	466^{+24}_{-20}	(c)	74.5 ± 1.7	15.241 ± 0.022
WISE-0825	WISE J082507.35+280548.5	(5)	387^{+15}_{-15}	(c)	152.6 ± 2.0	14.655 ± 0.024
WISE-0830	WISEA J083011.95+283716.0	(6)	367 ± 79	(a)	90.6 ± 13.7[a]	16.004 ± 0.072
WISE-1141	WISEA J114156.67–332635.5	(7)	460 ± 79	(a)	104.0 ± 2.9	14.632 ± 0.030
WISE-1206	WISE J120604.38+840110.6	(8)	472^{+26}_{-20}	(c)	84.7 ± 2.1	15.173 ± 0.023
WISE-1405	WISEPC J140518.40+553421.4	(3)	392^{+16}_{-15}	(c)	158.2 ± 2.6	14.098 ± 0.014
WISE-1446	CWISEP J144606.62–231717.8	(9)	351^{+16}_{-13}	(c)	103.8 ± 5.0	15.955 ± 0.072
WISE-1541	WISEPA J154151.66–225025.2	(3)	411^{+18}_{-17}	(c)	166.9 ± 2.0	14.218 ± 0.030
WISE-1639	WISEA J163932.75+184049.4	(9)	511 ± 79	(a)	61.9 ± 4.7	15.481 ± 0.036
WISE-1738	WISEPA J173835.53+273258.9	(3)	450 ± 88	(a)	130.9 ± 2.1	14.519 ± 0.017
WISE-2056	WISEPC J205628.90+145953.3	(3)	481^{+26}_{-20}	(c)	140.8 ± 2.0	13.925 ± 0.016
WISE-2220	WISE J222055.31–362817.4	(2)	452 ± 88	(a)	95.5 ± 2.1	14.807 ± 0.024
WISE-2354	WISEA J235402.79+024014.1	(8)	347^{+13}_{-11}	(c)	130.6 ± 3.3	15.018 ± 0.030
NIRISS F480M Imaging (Program ID 1230)						
UGPS-0722	UGPS J072227.51–054031.2	(10)	569 ± 45	(a)	242.8 ± 2.4	12.198 ± 0.008
WISE-0855	WISE J085510.83–071442.5	(11)	250 ± 50	(a)	439.0 ± 2.4	13.820 ± 0.029
NIRISS F480M Imaging (Program ID 1189)						
WISE-1828	WISEPA J182831.08+265037.8	(3)	406 ± 88	(a)	100.3 ± 2.0	14.393 ± 0.016

Notes. Discovery references are as follows: (1) D. J. Pinfield et al. (2014), (2) J. D. Kirkpatrick et al. (2012), (3) M. C. Cushing et al. (2011), (4) J. D. Kirkpatrick et al. (2013), (5) R. L. Griffith et al. (2012), (6) D. C. Bardalez Gagliuffi et al. (2020), (7) C. G. Tinney et al. (2014), (8) A. C. Schneider et al. (2015), (9) F. Marocco et al. (2020), (10) P. W. Lucas et al. (2010), (11) K. L. Luhman (2014).$T_{\rm eff}$ references are as follows: (a) J. D. Kirkpatrick et al. (2024), (b) J. D. Kirkpatrick et al. (2021), (c) S. A. Beiler et al. (2024). Parallaxes are from J. D. Kirkpatrick et al. (2021) except for WISE-1446, where the parallax is from S. A. Beiler et al. (2024). The W2 magnitudes are proper-motion-corrected values (`w2mpro_pm`) from the CatWISE2020 Catalog (F. Marocco et al. 2021), curated by IRSA.
[a] Updated astrometry for WISE-0830 is given in Table 4.

3. Data Reduction and Photometry

3.1. NIRCam

We downloaded the stacked images and associated catalogs constructed from the five dithered exposures (i2d.fits) processed by the Data Management System (DMS, version 1.9.6; H. Bushouse et al. 2022). The photometry catalogs produced by the default DMS level 3 pipeline contained anomalous magnitude entries for a few targets, which prompted us to revisit this step by performing our own aperture photometry using the `photutils` package (version 1.8.0; L. Bradley et al. 2023). For each filter (F480M/F150W), we first determined the centroid of the PSF by fitting a quadratic function in the 3×3 pixels around the pixel with peak intensity, then estimated the local sky level from statistics in an annulus with radii of 4.92/6.082 and 7.083/9.496 pixels around the PSF center and subtracted this level. Next, we performed aperture photometry by summing pixel flux within a radius of 3.757/3.199 pixels, defined in the CRDS reference file, `jwst_nircam_apcorr_0004.fits`, as the radius encompassing 70% of the PSF-encircled energy. Finally, we applied an aperture correction by multiplying the extracted flux by 1.4863/1.4485. This yielded flux measurements, F, expressed in megajansky/steradian that we converted to Vega magnitudes by applying the $\mathrm{mag_{AB}} - \mathrm{mag_{Vega}} = -3.85/-2.15$ mag offset (reference: `jwst_nircam_abstovegaoffset_0002.fits`) from the AB magnitude:

$$\mathrm{mag_{AB}} = -2.5 \log_{10}\left(\frac{F\,[\mathrm{MJy/sr}] \times T \times A\,[\mathrm{sr/pixel}]}{3631\,[\mathrm{Jy}] \times 10^{-6}\,[\mathrm{MJy/Jy}]}\right), \quad (1)$$

where T is the throughput calibration, PHOTMJSR = $1.456 \pm 0.006/2.338 \pm 0.021$, A is the steradian-to-pixel area conversion, and PIXAR_SR = $9.332 \times 10^{-14}/2.287 \times 10^{-14}$, found in the `jwst_nircam_photom_0153/0150.fits` reference file.

The measurement uncertainty considers the readout noise and photon noise given as a pixel map by the DMS pipeline (the ERR extension of the cal.fits) but also includes the uncertainty in subtracting the background level. These combine to very small statistical errors of order 0.08% (F480M) and 0.2%–2% (F150W). The absolute flux calibration uncertainty is added in quadrature and, with a precision of 0.4% in the F480M, dominates the error budget for the photometric measurements reported in Table 2. For the F150W filter, the

Table 2
F150W and F480M Photometry of Our Y-dwarf Sample

Short Name	Observing Date Mid Exposure (UT)	Int. Time (minutes)	F150W (Vega mag)	F480M (Vega mag)
WISE-0304	2022-09-23T21:58:02	89.5	21.872 ± 0.010	15.428 ± 0.005
WISE-0336AB	2022-09-22T13:13:10	40.3	22.038 ± 0.012	14.538 ± 0.005
WISE-0336A[a]	2022-09-22T13:13:10	40.3	22.114 ± 0.016	$14.727^{+0.054}_{-0.023}$
WISE-0336B[a]	2022-09-22T13:13:10	40.3	$24.938^{+0.175}_{-0.105}$	$16.534^{+0.120}_{-0.252}$
WISE-0359	2022-09-23T17:51:38	89.5	22.281 ± 0.010	15.268 ± 0.005
WISE-0410	2022-09-23T23:43:56	26.8	20.167 ± 0.010	13.999 ± 0.005
WISE-0535	2022-06-27T22:27:30	62.6	22.866 ± 0.013	14.795 ± 0.005
WISE-0647	2022-11-11T16:38:29	58.2	23.332 ± 0.013	14.919 ± 0.005
WISE-0713	2022-11-12T08:42:33	31.3	20.445 ± 0.010	14.183 ± 0.005
UGPS-0722[b]	2023-04-17T22:33:44	18.9	17.26 ± 0.03	12.016 ± 0.011
WISE-0734	2022-06-28T00:07:35	76.1	21.706 ± 0.011	15.162 ± 0.004
WISE-0825	2022-11-12T10:10:45	40.3	22.831 ± 0.014	14.418 ± 0.005
WISE-0830	2022-11-12T22:49:59	120.8	25.261 ± 0.026	15.644 ± 0.005
WISE-0855[b]	2022-11-19T09:25:29	36.5	23.98 ± 0.10	13.679 ± 0.011
WISE-1141	2023-06-29T22:27:31	40.3	20.580 ± 0.010	14.582 ± 0.005
WISE-1206	2023-02-27T21:31:43	71.6	21.227 ± 0.010	15.112 ± 0.005
WISE-1405	2023-03-02T12:43:40	25.1	21.756 ± 0.012	13.930 ± 0.005
WISE-1446	2023-03-02T09:15:03	143.2	23.672 ± 0.013	15.694 ± 0.005
WISE-1541	2023-03-02T11:18:04	28.6	22.004 ± 0.011	14.018 ± 0.005
WISE-1639	2023-06-28T21:47:19	13.4	21.316 ± 0.014	13.487 ± 0.005
WISE-1738	2022-06-29T17:21:58	31.3	20.365 ± 0.010	14.464 ± 0.005
WISE-1828[b]	2022-07-28T17:52:53	35.8	23.07 ± 0.10	14.242 ± 0.011
WISE-2056	2023-06-28T09:03:58	22.4	20.057 ± 0.001	13.762 ± 0.005
WISE-2220	2023-07-01T21:31:28	49.2	21.161 ± 0.011	14.745 ± 0.005
WISE-2354	2022-06-29T19:09:18	58.2	23.098 ± 0.013	14.930 ± 0.005

Notes.
[a] The individual F150W and F480M magnitudes for the WISE-0336 system were determined from the aperture photometry for the unresolved system and the flux ratios for each component measured by P. Calissendorff et al. (2023).
[b] The F150W magnitudes for UGPS-0722, WISE-0855, and WISE-1828 were synthesized from spectroscopic observations by P. W. Lucas et al. (2010), K. L. Luhman et al. (2024), and M. C. Cushing et al. (2021). Uncertainties for these values were estimated to be equal to the spectral flux calibration uncertainty.

absolute calibration uncertainty, 0.9%, is comparable to the statistical noise.

3.2. Photometry of the Binary WISE-0336A+B

We present updated photometry for both components of the known binary WISE-0336A/B from that reported in P. Calissendorff et al. (2023). We treated the A+B components as unresolved to obtain the aperture photometry of the system in exactly the same manner as for the other NIRCam targets. We then used the binary contrast published in P. Calissendorff et al. (2023) of $\Delta F480M = F480M_B - F480M_A = 1.81^{+0.14}_{-0.31}$ and $\Delta F150W = F150W_B - F150W_A = 2.82^{+0.19}_{-0.11}$ to calculate the magnitude of each component separately. The uncertainties were propagated using a Monte Carlo simulation of 5×10^5 realizations. Results are resilient to aperture size selection.

3.3. NIRISS

We reprocessed the data with the DMS (version 1.12.5), enabling the `charge_migration` step, up to the end of level 2, which produced cal.fits images. Then we ran a custom $1/f$ correction on the three data sets observed in FULL mode (both WISE-0855 and WISE-1828 observations) while using directly the cal.fits for UGPS-0722 because the $1/f$ imprint is less pronounced on the SUB80 images. Using the custom $1/f$-corrected data changed the photometry by less than 1% compared to using the cal.fits directly.

To extract photometry of NIRISS F480M images, we adopted the same procedure as performed on the NIRCam data sets and used by the DMS pipeline. We used the prescribed aperture and sky annulus radii of 4.68, 7.80, and 11.74 pixels, respectively, while the aperture correction was 1.458 (70% encircled energy), found in jwst_niriss_apcorr_0008.fits. The AB to Vega magnitude offset was $mag_{AB} - mag_{Vega} = -3.4268$, the PHOTMJSR $= 1.220 \pm 0.013$, and the PIXAR_SR $= 1.009 \times 10^{-13}$ (jwst_niriss_abstovegaoffset_0003.fits, jwst_niriss_photom_0043.fits). The photometry has very small statistical errors of order 0.07%. The absolute flux calibration uncertainty is added in quadrature and, with a precision of 1.04%, dominates the error budget for the F480M photometric measurements reported in Table 2.

In order to compare the colors of these three NIRISS sources to the rest of our sample, we synthesized F150W photometry from available near-infrared spectra (P. W. Lucas et al. 2010; K. L. Luhman 2014; M. C. Cushing et al. 2021). The JWST user documentation supplies filter transmissions which include the instrument system throughput for each camera; we used the F150W NIRCam transmission for consistency with the other measurements. For reference, we explored the differences between the NIRCam and NIRISS photometric systems by synthesizing F150W and F480M magnitudes for each camera for five Y dwarfs with JWST spectra across the bandpasses (S. A. Beiler et al. 2024). The five Y dwarfs had a range in T_{eff} of 350–500 K, and the differences in the photometry were small, with no trend seen with T_{eff}. We found an average

Table 3
Astrometry for the NIRCam Sample

Short Name	MJD (days)	α_{2000} (deg(mas))	δ_{2000} (deg(mas))	No. of Gaia Anchors	Offset from K21 Model		
					α (mas)	δ (mas)	σ[a]
WISE-0304	59845.91531	46.2048671(20.0)	−27.0839387(15.8)	4	13.9 ± 21.7	−37.3 ± 19.7	2.0
WISE-0336	59844.55082	54.0202647(16.4)	−1.7351151(15.2)	6	−18.4 ± 17.9	−12.3 ± 16.7	1.3
WISE-0359	59845.74420	59.8912978(15.0)	−54.0343645(15.2)	3	2.6 ± 15.7	−3.8 ± 16.4	0.3
WISE-0410	59845.98885	62.5983013(15.8)	15.0390435(19.0)	4	3.1 ± 17.1	1.3 ± 20.0	0.2
WISE-0535	59757.93577	83.8183968(18.2)	−75.0066568(16.7)	110	4.2 ± 19.1	25.5 ± 17.9	1.4
WISE-0647	59894.69340	101.8468599(15.4)	−62.5418782(17.4)	13	10.5 ± 15.9	−5.7 ± 17.9	0.7
WISE-0713	59895.36289	108.3454431(16.6)	−29.2992193(17.4)	98	−4.6 ± 18.0	−17.7 ± 18.6	1.0
WISE-0734	59758.00527	113.6771949(16.6)	−71.9624680(16.9)	14	0.7 ± 16.9	−6.8 ± 17.4	0.4
WISE-0825	59895.42414	126.2804168(15.5)	28.0959557(15.9)	7	5.5 ± 17.0	−4.5 ± 17.2	0.4
WISE-0830	59895.95138	127.5492249(29.2)	28.6142199(23.1)	4	182.9 ± 309.9[b]	112.1 ± 198.7[b]	0.8
WISE-1141	60124.93578	175.4823320(18.6)	−33.4434263(20.2)	15	32.7 ± 22.2	−12.7 ± 23.5	1.6
WISE-1206	60002.89703	181.4985345(16.0)	84.0186397(23.0)	3	2.0 ± 17.7	16.9 ± 24.0	0.7
WISE-1405	60005.53033	211.3120210(16.9)	55.5733955(15.1)	4	−1.0 ± 19.3	13.2 ± 16.8	0.8
WISE-1446	60005.38545	221.5254686(20.8)	−23.2903901(15.6)	14	195.8 ± 323.1	113.0 ± 168.5	0.9
					52.4 ± 85.4[c]	60.9 ± 80.8[c]	1.0[b]
WISE-1541	60005.47089	235.4616164(17.1)	−22.8407867(17.1)	31	3.7 ± 18.6	29.7 ± 18.6	1.6
WISE-1639	60123.90787	249.9258850(16.3)	−68.8055121(15.8)	106	−4.4 ± 18.4	−24.3 ± 18.1	1.4
WISE-1738	59759.72360	264.6493275(16.4)	27.5485376(15.6)	19	−7.9 ± 17.4	8.9 ± 16.8	0.7
WISE-2056	60123.37776	314.1235676(16.5)	15.0000852(16.2)	44	19.1 ± 17.8	3.0 ± 17.6	1.1
WISE-2220	60126.89686	335.2318522(21.2)	−36.4718910(17.5)	6	−0.6 ± 22.7	−3.0 ± 18.9	0.2
WISE-2354	59759.79813	358.5132467(20.6)	2.6693245(16.3)	3	−46.6 ± 24.0	−39.8 ± 20.3	2.8

Notes.
[a] The last column (Offset from K21 Model - σ) compares the measured and modeled positions and expresses the offset in units of the combined model + measurement uncertainties.
[b] For WISE-0830 the model was updated; results are given in Table 4.
[c] For WISE-1446, comparison with the model of F. Marocco et al. (2025, in preparation) shows good agreement and improved precision.

difference for NIRCam – NIRISS of ΔF150W = −0.040 ± 0.012 and ΔF480M = –0.010 ± 0.001 mag. Any systematic difference due to the different F480M throughput for the two cameras is therefore similar in size to the absolute flux calibration uncertainty.

4. Astrometry: Proper Motion and Parallax

The most recent parallax measurements place the brown dwarfs of our sample at a distance of 16 pc or closer to the Sun. All have significant proper motion, mostly derived from Spitzer observations obtained between 2010 and 2019 (J. D. Kirkpatrick et al. 2021). Our JWST observations obtained in 2022 and 2023 can therefore test the published astrometry by extrapolating the proper motion and parallax model over a 3–4 yr time frame.

To propagate the motion of our targets' proper motion and parallax, we use the SkyCoord module of Astropy and convert celestial coordinates to the Geocentric Celestial Reference System (or GCRS). To eliminate the annual aberration, which is the dominant motion, we measure angular positions relative to a virtual distant reference point at the celestial position of each target. We neglect the parallax due to JWST being at the Lagrange point 2, which introduces parallax errors of less than 1%, or typically ~1 mas at the distance of our targets.

The initial position measurements of all sources including the brown dwarfs (`RA_ICRS`, `DE_ICRS`) come from the catalog produced by the default DMS level 3 product on the stacked frame. We downloaded the most recent version of the catalogs found on MAST, based on the calibration software version 1.15.1. In each field, the astrometry is then anchored on available Gaia Data Release 2 sources (from 3 to 100), taking proper motion and parallax into account. Experimentations with four targets having more than 40 Gaia stars in the NIRCam field of view show that, after applying an offset in R. A. and decl., residuals appear unstructured with no obvious rotation or scale pattern. Also, for about half our targets there is insufficient Gaia-measured stars ($\leqslant$7) to confidently constrain the four-parameter affine transformation (offsets, rotation, scale). Therefore, for the purpose of this astrometry check, anchoring only considers R.A. and decl. offsets. Anchoring uncertainties range between 15 and 29 mas per axis (see Table 3).

As our baseline model for the brown dwarf astrometry, we adopt the J. D. Kirkpatrick et al. (2021, hereafter K21 in the text and figures) proper motion and parallax. In the case of WISE-1446, we adopt the more precise parallax and proper motion measurements of F. Marocco et al. (2025, in preparation). These models include an epoch of reference, t_0, and corresponding celestial positions, $\alpha_{\rm ICRS}$, $\delta_{\rm ICRS}$ at t_0. To check predictions of the model, we propagate the target position to the epoch of our JWST observation and compare it with our measured position. The propagated position uncertainties are obtained by performing a Monte Carlo simulation using 1000 trials. The uncertainty of each model parameter (parallax, proper motion, t_0, $\alpha_{\rm ICRS}$, and $\delta_{\rm ICRS}$) is assumed to be a Gaussian distribution centered on the parameter value. For all but one brown dwarf, WISE-2354, we confirm that the position of the target in the JWST images agrees with predicted positions within 2σ. The disagreement for WISE-2354 is at the 2.8σ level. That is too small to impact future JWST follow-ups, as in absolute terms the error is well under 100 mas, or roughly one NIRCam long-wave pixel.

Table 4
Updated Spitzer + JWST Astrometry Model for WISEA J083011.95 +283716.0

Model Parameter		Value ($\chi^2_\nu = 0.749$, 18 Data Points)
Epoch	(t_0)	58850 (MJD)
R.A. at t_0	(α_{ICRS})	$127.549366° \pm 6.8$ mas
Decl. at t_0	(δ_{ICRS})	$28.615822° \pm 5.6$ mas
Parallax	(ϖ)	99.2 ± 6.5 mas
P.M. R.A.	($\mu_{R.A.}$)	-190.2 ± 8.4 mas yr^{-1}
P.M. Decl.	($\mu_{Decl.}$)	-2011.0 ± 6.9 mas yr^{-1}

In general, the propagated model uncertainties at the epoch of our JWST observation (2022) are very small (4–12 mas per axis). However, the K21 model for two brown dwarfs, WISE-0830 and WISE-1446, has a large total uncertainty of $\geqslant$350 mas. In the case of WISE-0830, we decided to update the model because even a single JWST measurement offered the opportunity to improve its precision, especially as the JWST measurement happened to sample a parallax peak. We ran the existing tool described in J. D. Kirkpatrick et al. (2019, 2021) by combining this measurement to the existing suite of Spitzer and Wide-field Infrared Survey Explorer (WISE) measurements already available. The JWST spacecraft barycentric (*XYZ*) position was considered in our calculations. Results are presented in Table 4. The new parallax places WISE-0830 at a distance of $10.1^{+0.7}_{-0.6}$ pc, about 10% closer than previously thought ($11.0^{+2.0}_{-1.5}$ pc). For WISE-1446, we were able to test a recent and more precise astrometry model (F. Marocco et al. 2025, in preparation), which shows a better agreement with our observation and has an improved precision of $\leqslant$100 mas.

5. Brown Dwarf Colors

Figure 1 shows a color–magnitude diagram, with the new data presented here as black filled circles. Our homogeneous JWST photometry confirms the large intrinsic scatter ($\sim$1 mag) previously seen for Y dwarfs in color–magnitude diagrams (e.g., J. D. Kirkpatrick et al. 2021; S. K. Leggett et al. 2021), which excludes measurement noise or filter transformations as an explanation.

Other filled circles in Figure 1 represent F150W and F480M colors synthesized from spectra by S. A. Beiler et al. (2024, their Tables 7 and 9), using NIRCam bandpasses. The symbol color indicates the $T_{\rm eff}$ value determined by S. A. Beiler et al. (2024) via bolometric luminosities determined from empirical spectral energy distributions built with MIRI and NIRSpec spectra. Colored rings around black points indicate the S. A. Beiler et al. (2024) $T_{\rm eff}$ values for those sources. The empirical S. A. Beiler et al. (2024) $T_{\rm eff}$ range for each symbol color is indicated along the right axis of the top-left panel.

5.1. Comparison to Models

We compare the photometry to synthetic photometry calculated by four cool brown dwarf models, each based on different atmosphere prescriptions. As a baseline model, the Sonora Bobcat models assume equilibrium chemistry (M. S. Marley et al. 2021). But, given the evidence for out-of-equilibrium chemistry in the atmosphere of ultracool dwarfs, the Sonora Elf Owl models include disequilibrium chemistry (S. Mukherjee et al. 2024), the ATMO2020++ models use disequilibrium chemistry and introduce adjustments to the adiabat profile (S. K. Leggett & P. Tremblin 2023), while B. Lacy & A. Burrows (2023) introduce water clouds in their disequilibrium models because the atmospheres of the coldest Y dwarfs, those with $T_{\rm eff} \lesssim 400$ K, are cold enough for water to condense (e.g., C. V. Morley et al. 2014). We note that the Sonora Cholla (T. Karalidi et al. 2021) and Diamondback (C. V. Morley et al. 2024) models do not include atmospheres as cold as those of the Y dwarfs.

All model sequences in Figure 1 are cloud-free except for the B. Lacy & A. Burrows (2023) sequence shown in the bottom-right panel. Solar and subsolar metallicities are included. Surface gravities of $\log g = 4.0$ cm s^{-2} and 4.5 cm s^{-2} are shown. From evolutionary models we estimate that field dwarfs with ages of 2 to 4 Gyr have $\log g \approx 4.5$ cm s^{-2} for $325 \lesssim T_{\rm eff}$ K $\lesssim 550$ and $\log g \approx 4.0$ cm s^{-2} for $200 \lesssim T_{\rm eff}$ K $\lesssim 325$ (M. S. Marley et al. 2021). Model sequences' line types indicate metallicity and gravity, as shown in the legend in the top-right panel.

Figure 1 indicates that the ATMO2020++ (M. W. Phillips et al. 2020; S. K. Leggett et al. 2021; A. M. Meisner et al. 2023; S. K. Leggett & P. Tremblin 2025) and the B. Lacy & A. Burrows (2023) models reproduce the observed colors better than the Sonora Bobcat or Elf Owl models (M. S. Marley et al. 2021; S. Mukherjee et al. 2024). The $T_{\rm eff}$ values from the ATMO2020++ and the B. Lacy & A. Burrows (2023) models are also in good agreement with the values measured by S. A. Beiler et al. (2024) from the observed luminosities, while the Bobcat and Elf Owl models are not.

For brown dwarfs warmer than 350 K, the Sonora Bobcat F150W – F480M colors appear to be too red, while the Elf Owl colors appear to be too blue (assuming that this local sample of brown dwarfs is not unusually metal-poor). The likely cause of the red Bobcat color is the exclusion of disequilibrium chemistry, which increases the abundance of CO and CO_2 (e.g., K. J. Zahnle & M. S. Marley 2014) that absorb light at $\lambda \approx 4.7$ μm and 4.2 μm, respectively (e.g., Z. Tu et al. 2024, their Figure 5), thereby decreasing the F480M flux. The likely cause of the blue Elf Owl color is an excess of near-infrared flux at F150W; it seems that standard radiative-convective atmospheres for cold brown dwarfs produce an excess of energy in the near-infrared (e.g., S. K. Leggett et al. 2017, 2021; T. Karalidi et al. 2021), which is the issue that the ATMO2020++ models address empirically by changing the pressure–temperature profile such that the deeper regions, where the near-infrared energy emerges, is colder. Although empirical, the adjustment is physically motivated by thermal changes due to rapid rotation and/or chemical changes in the deep layers due to condensation (e.g., S. K. Leggett et al. 2021; S. K. Leggett & P. Tremblin 2025).

The ATMO2020++ sequence does appear to show a systematic offset in color. This may be partly due to the definition of the F150W bandpass. For cold brown dwarfs the signal through this filter comes only from the narrow *H*-band flux peak at the extreme red of the bandpass. Hence, the color is sensitive to the definition of the red cutoff of the filter.

The ATMO2020++ and the B. Lacy & A. Burrows (2023) models calculate that the F480M absolute magnitude is a good indicator of $T_{\rm eff}$ for 275–600 K brown dwarfs because of its relatively small dependence on metallicity and gravity ($\Delta M_{\rm F480M} \sim 0.3$ mag for $\Delta \log g$ or Δ[m/H] ~ 0.5 dex); compare the *y*-axis locations of the plus symbols in Figure 1. On the other hand, these models calculate that the F150W – F480M color is sensitive to both gravity and metallicity ($\Delta(\mathtt{F150W} - \mathtt{F480M}) \sim 1.0$ mag for $\Delta \log g$ or Δ[m/H] ~ 0.5 dex); compare the *x*-axis locations of the plus symbols in Figure 1.

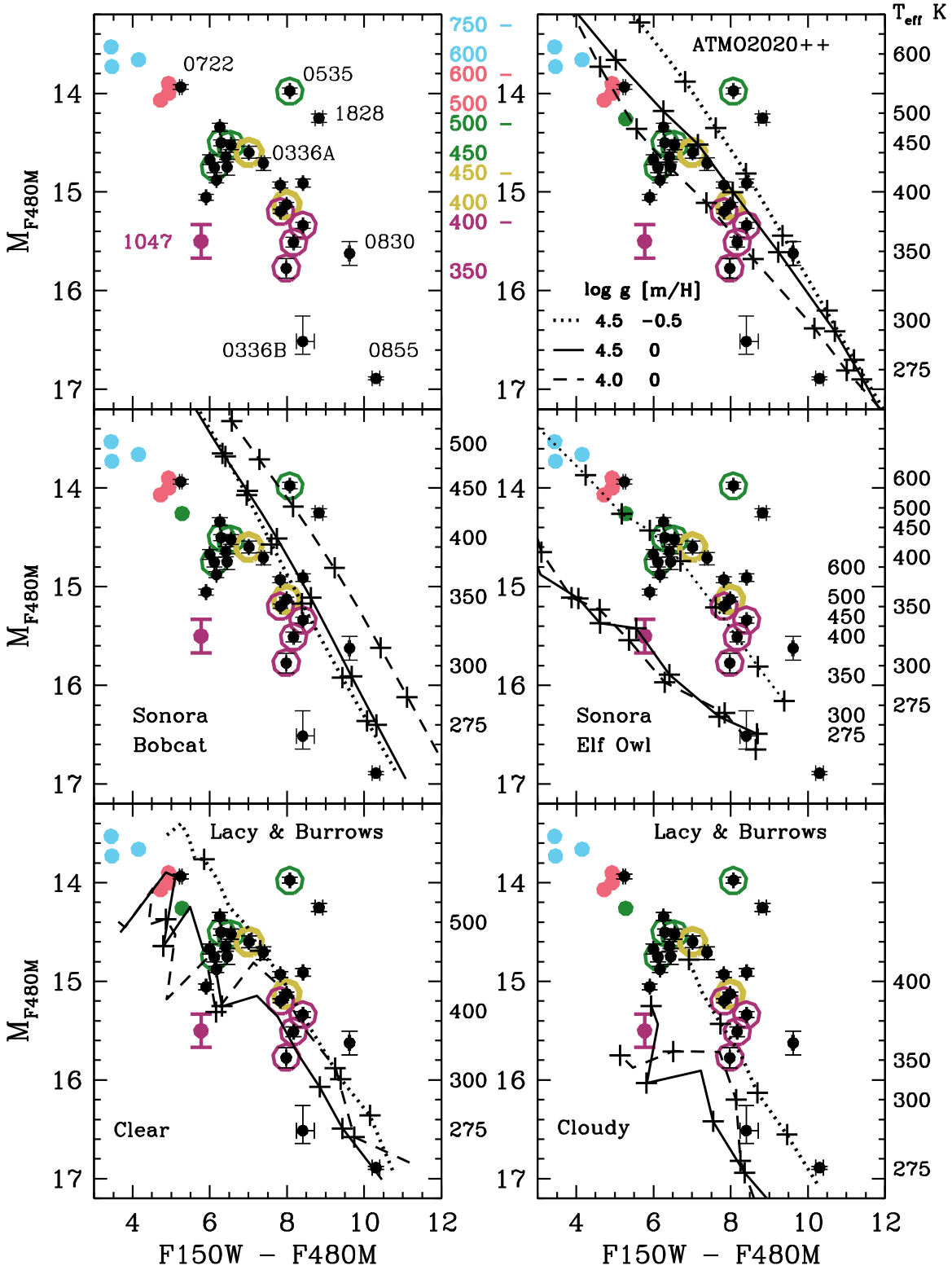

Figure 1. F480M vs. F150W – F480M color–magnitude diagrams. Black circles represent new measurements presented here. Colored dots are synthesized colors from S. A. Beiler et al. (2024) where the symbol color indicates $T_{\rm eff}$, determined by Beiler et al. from luminosity measurements. Colored rings similarly indicate $T_{\rm eff}$; the symbol color for a given $T_{\rm eff}$ range is indicated along the right axis of the top-left panel. The warmest and coldest objects in our sample, the WISE-0336 binary system, and outliers, are identified in the top-left panel. The other panels compare the data to various model sequences; surface gravity and metallicity properties are indicated by line type as shown in the legend in the top-right panel. Sequences in the top-right panel are from disequilibrium-chemistry and adiabat-adjusted ATMO2020++ models (S. K. Leggett et al. 2021; A. M. Meisner et al. 2023). The middle panels show Sonora sequences, equilibrium-chemistry Bobcat on the left (M. S. Marley et al. 2021) and disequilibrium-chemistry Elf Owl on the right (S. Mukherjee et al. 2024). The bottom panels show disequilibrium-chemistry models from B. Lacy & A. Burrows (2023) with and without water clouds. Model $T_{\rm eff}$ values are indicated along the right axes and plus symbols along the model sequences indicate colors at those $T_{\rm eff}$. For the Elf Owl panel the outer axis $T_{\rm eff}$ values refer to the metal-poor sequence and the inner values to the solar-metallicity sequences; for the other models the M_{480M} values are more similar across the metallicity range.

5.2. Superluminous or Very Red Brown Dwarfs

WISE-0535 and WISE-1828 appear to be superluminous and/or redder than the other dwarfs in Figure 1. WISE-0830 may be a colder example of this group. We discuss each of these brown dwarfs individually below, in R.A. order.

A preliminary analysis of the spectral distribution of WISE-0535 using ATMO2020++ synthetic spectra by S. K. Leggett & P. Tremblin (2024) indicates that its superluminosity is due to multiplicity. We address this further in our companion paper (T. Vandal et al. 2025, in preparation).

This work and Matuszewska et al. (2025, in preparation) present the first near-infrared detection of the cold brown dwarf WISE-0830. Its location in Figure 1 suggests that it is a typical field dwarf with $T_{\rm eff} \approx 350$ K. However, WISE-0830 may be superluminous, depending on the (currently poorly defined) color–magnitude trend for the coldest objects. Superluminosity suggests lower metallicity, higher gravity (older age), or multiplicity. WISE-0830 has the highest tangential velocity in our sample (108 km s^{-1}; D. C. Bardalez Gagliuffi et al. 2020), possibly supporting an older age and lower metallicity for this Y dwarf compared to typical field dwarfs.

The extreme colors of WISE-1828 may indicate that it is multiple, has a high gravity, or is metal-poor. Recent studies using JWST imaging data find no evidence of a companion at separations >0.5 au (M. De Furio et al. 2023). Recent spectral analyses of JWST NIRSpec and MIRI data by B. W. P. Lew et al. (2024) and D. Barrado et al. (2023) find that the metallicity is approximately solar, and that the luminosity is consistent with evolutionary models if the system is a tight binary—an order-of-magnitude estimate by B. W. P. Lew et al. (2024), based on the radial velocity, suggests a separation of 20 Jupiter radii. S. K. Leggett & P. Tremblin (2025) find a good fit to the JWST NIRSpec and MIRI data with ATMO2020++ solar-metallicity models if the system is an equal-mass binary with unusually high gravity, i.e., a relatively massive and old system.

5.3. A Blue Candidate Very Young Jupiter-mass Brown Dwarf

CWISEP J104756.81+545741.6 (hereafter WISE-1047, identified as "1047" in Figure 1) is not in our imaging sample, but is in the spectroscopic sample of S. A. Beiler et al. (2024), who synthesize JWST colors. S. A. Beiler et al. (2024) also provide a trigonometric parallax measurement for WISE-1047, whose discovery is presented in A. M. Meisner et al. (2020). S. A. Beiler et al. (2024) measure a parallax of 68.1 ± 4.9 mas, and calculate apparent magnitudes from their spectra of F150W = 22.10 and F480M = 16.33; the NIRSpec absolute calibration uncertainty is estimated to be less than 3% or 0.03 mag.[23]

Figure 1 shows that WISE-1047 is blue or subluminous. Z. Tu et al. (2024) point out that the JWST spectra for this Y dwarf show unusually strong CO_2 and CO absorption (see their Figure 4). Atmospheric models calculate that decreasing gravity results in increasing CO and CO_2 absorption, and that these features are less sensitive to changes in metallicity (T. Karalidi et al. 2021; B. Lacy & A. Burrows 2023; S. K. Leggett & P. Tremblin 2025). The bandpass of the F480M filter directly samples the CO absorption, making it a useful indicator of the strength of this feature, an effect which could be masked by a broader filter.

Figure 1 suggests $\log g \ll 4.0$ and $T_{\rm eff} \approx 400$ K for WISE-1047. Evolutionary models (e.g., M. S. Marley et al. 2021) then suggest a mass less than 3 $M_{\rm Jup}$ and an age less than 0.2 Gyr for this Y dwarf. Taking the proper motion for this source from J. D. Kirkpatrick et al. (2021) and the parallax from S. A. Beiler et al. (2024), the BANYAN Σ tool (J. Gagné et al. 2018) calculates a 52% likelihood that WISE-1047 is a member of the Argus association, which has an age of ∼40 Myr (B. Zuckerman 2018). If this brown dwarf is indeed this young, then its mass is only 1 $M_{\rm Jup}$ and $\log g \approx 3.3$. Further improvement to the distance measurement and a radial velocity measurement would be useful for this object.

5.4. The Coldest Brown Dwarfs and Water Clouds

Water clouds are first expected to impact the photosphere when brown dwarfs cool to $T_{\rm eff} \sim 350$ K (e.g., A. Burrows et al. 2003; C. V. Morley et al. 2014; B. Lacy & A. Burrows 2023). The B. Lacy & A. Burrows (2023) disequilibrium-chemistry sequences shown in Figure 1 are for clear atmospheres and for atmospheres with thin water clouds at pressures of 0.4 bar with a particle size of 10 μm (E10 type). The addition of clouds makes F150W brighter and F480M fainter (B. Lacy & A. Burrows 2023), resulting in the bluer F150W – F480M colors seen in Figure 1.

The coldest objects in our sample are WISE-0336B and WISE-0855, with $T_{\rm eff} \lesssim 300$ K. The WISE-0336 binary components are separated by 0.″09, or 1 au (P. Calissendorff et al. 2023). The reanalysis of the photometry for the system presented here produces colors within 0.07 magnitudes of the P. Calissendorff et al. (2023) values. Figure 1 suggests that WISE-0336A is a typical field Y dwarf, with $T_{\rm eff}$ between 400 and 450 K, and that WISE-0336B is slightly warmer than WISE-0855 but colder than the other Y dwarfs in the sample, with $T_{\rm eff}$ between 275 and 300 K. If the system has an age of ∼2 Gyr (e.g., W. M. J. Best et al. 2024), then the component masses are approximately 12 and 5 $M_{\rm Jup}$ (M. S. Marley et al. 2021).

Interestingly, WISE-0336B is significantly bluer than WISE-0855. Given that WISE-0336A appears to have a gravity and metallicity typical of the field, the bluer color for 0336B is unlikely to be due to an unusually low gravity or high metallicity. Instead, the B. Lacy & A. Burrows (2023) models suggest the difference is either that the atmosphere of WISE-0336B is cloudy and that of WISE-0855 is clear, or that WISE-0855 is cloudy but has a significantly higher gravity and/or lower metallicity than WISE-0336B. Recent analyses of JWST data for WISE-0855 support the former scenario, as H. Kühnle et al. (2024) find no evidence of water clouds, and the metallicity and gravity appears typical of the field (K. L. Luhman et al. 2024; H. Kühnle et al. 2024). The detection of water clouds may also be dependent on the surface gravity of the brown dwarf or on the viewing angle: Observations of L dwarfs suggest that the vertical extent of the water clouds is dependent on gravity (G. Suárez et al. 2023; G. Suárez & S. Metchev 2023), and the structured nature of surface storms and clouds results in colors being dependent on viewing angle (J. M. Vos et al. 2017).

[23] https://jwst-docs.stsci.edu/jwst-calibration-status/nirspec-calibration-status/nirspec-fixed-slit-calibration-status##NIRSpecFixedSlitCalibrationStatus-Photometricrepeatability&gsc.tab=0

6. Conclusions

We share one of the first homogeneous photometric data sets of Y-type brown dwarfs observed with JWST. The sample consists of 20 Y dwarfs observed with NIRCam in F150W and F480M simultaneously, and three Y dwarfs observed with NIRISS in F480M. We present an F480M versus F150W – F480M color–magnitude diagram, which confirms that Y dwarfs have a large ∼1 mag scatter at a given near-infrared −5 μm color, as noted in previous studies.

Of the different atmosphere models (Sonora Bobcat, Sonora Elf Owl, ATMO2020++, and B. Lacy & A. Burrows 2023), ATMO2020++ and that of Lacy & Burrows best reproduce the colors of the 350–500 K Y dwarfs overall, while the cloudy and clear Lacy & Burrows models reproduce the colors of the 300 K objects best. Both cloudy and clear atmospheres seem to be required to explain the observed colors of the coldest Y dwarfs.

We provide a photometry update for the Y+Y binary brown dwarf WISE-0336A/B, and find that only the cloudy Lacy & Burrows model reproduces the colors of the faint secondary WISE-0336B. WISE-0336B appears to be a cloudy version of WISE-0855, with $T_{\rm eff} \lesssim 300$ K.

We jointly present here and in Matuszewska et al. (2025, in preparation) the first near-infrared detection of WISE-0830 and confirm its extremely red F150W – F480M color (Figure 1, top-left panel). The red color may be an indication of low metallicity and/or high gravity (i.e., an older-than-average age) for this high-velocity Y dwarf.

The F480M filter is particularly sensitive to the CO absorption band at $\lambda \approx 4.7$ μm. We find that one of the 400 K Y dwarfs in the S. A. Beiler et al. (2024) sample, WISE-1047, is unusually blue in F150W – F480M, and Z. Tu et al. (2024) note that the spectrum of this brown dwarf has unusually strong CO (and CO_2) absorption. This spectral signature is indicative of low gravity according to atmospheric models, and the BANYAN Σ tool (J. Gagné et al. 2018) calculates a 52% likelihood that WISE-1047 is a member of the ∼40 Myr old Argus association; evolutionary models then imply that the object is extremely low mass, only ∼1 $M_{\rm Jup}$.

Finally, the astrometry at the JWST observation epoch is measured and we find agreement within 2σ with the proper motion and parallax models of J. D. Kirkpatrick et al. (2021) and F. Marocco et al. (2025, in preparation), apart from one target, WISE-2354. The 2.8σ disagreement for WISE-2354 is nevertheless smaller than a NIRCam long-wave pixel. We updated the astrometry model of WISE-0830 by folding in our NIRCam measurement to reduce its parallax uncertainty by a factor of 2. This now puts WISE-0830 at a slightly smaller distance than previously measured of $10.1^{+0.7}_{-0.6}$ pc.

Acknowledgments

L.A. acknowledges support from the Canadian Space Agency funding program #22JWGO1-11. M.R.M., P.C., D.C.B.G., C.A.B., A.J.B., and J.A.G. gratefully acknowledge support through NASA grant No. JWST-GO-02473.002-A. M. D.F. is supported by an NSF Astronomy and Astrophysics Postdoctoral Fellowship under award AST-2303911. T.R would like to acknowledge support from NASA through the JWST NIRCam project through contract number NAS5-02105 (PI: M. Rieke, University of Arizona). C.F. acknowledges support from the Trottier Family Foundation and the Trottier Institute for Research on Exoplanets through her Trottier Postdoctoral Fellowship. Part of the work by C.A.B. was carried out at the Jet Propulsion Laboratory, California Institute of Technology, under a contract with the National Aeronautics and Space Administration (grant No. 80NM0018D0004). This work was authored by A.Z.G. of Caltech/IPAC under Contract No. 80GSFC21R0032 with the National Aeronautics and Space Administration. This research made use of `Photutils`, an Astropy package for detection and photometry of astronomical sources (L. Bradley et al. 2023).

ORCID iDs

Loïc Albert https://orcid.org/0000-0003-0475-9375
Sandy K. Leggett https://orcid.org/0000-0002-3681-2989
Per Calissendorff https://orcid.org/0000-0002-5335-0616
Thomas Vandal https://orcid.org/0000-0002-5922-8267
J. Davy Kirkpatrick https://orcid.org/0000-0003-4269-260X
Daniella C. Bardalez Gagliuffi https://orcid.org/0000-0001-8170-7072
Matthew De Furio https://orcid.org/0000-0003-1863-4960
Michael Meyer https://orcid.org/0000-0003-1227-3084
Charles A. Beichman https://orcid.org/0000-0002-5627-5471
Adam J. Burgasser https://orcid.org/0000-0002-6523-9536
Michael C. Cushing https://orcid.org/0000-0001-7780-3352
Jacqueline Kelly Faherty https://orcid.org/0000-0001-6251-0573
Clémence Fontanive https://orcid.org/0000-0002-2428-9932
Christopher R. Gelino https://orcid.org/0000-0001-5072-4574
John E. Gizis https://orcid.org/0000-0002-8916-1972
Alexandra Z. Greenbaum https://orcid.org/0000-0002-7162-8036
Frantz Martinache https://orcid.org/0000-0003-1180-4138
Mamadou N'Diaye https://orcid.org/0000-0002-1721-3294
Benjamin J. S. Pope https://orcid.org/0000-0003-2595-9114
Thomas L. Roellig https://orcid.org/0000-0002-6730-5410
Johannes Sahlmann https://orcid.org/0000-0001-9525-3673
Anand Sivaramakrishnan https://orcid.org/0000-0003-1251-4124
Marie Ygouf https://orcid.org/0000-0001-7591-2731

References

Bardalez Gagliuffi, D. C., Faherty, J. K., Schneider, A. C., et al. 2020, ApJ, 895, 145
Barrado, D., Mollière, P., Patapis, P., et al. 2023, Natur, 624, 263
Beiler, S. A., Cushing, M. C., Kirkpatrick, J. D., et al. 2024, ApJ, 973, 107
Best, W. M. J., Sanghi, A., Liu, M. C., Magnier, E. A., & Dupuy, T. J. 2024, ApJ, 967, 115
Bowler, B. P., Blunt, S. C., & Nielsen, E. L. 2020, AJ, 159, 63
Bradley, L., Sipőcz, B., Robitaille, T., et al. 2023, astropy/photutils: v1.8.0, doi:10.5281/zenodo.7946442
Burrows, A., Hubbard, W. B., Lunine, J. I., & Liebert, J. 2001, RvMP, 73, 719
Burrows, A., Sudarsky, D., & Lunine, J. I. 2003, ApJ, 596, 587
Bushouse, H., Eisenhamer, J., Dencheva, N., et al. 2022, JWST Calibration Pipeline, v1.8.2, Zenodo, doi:10.5281/zenodo.7325378
Calissendorff, P., De Furio, M., Meyer, M., et al. 2023, ApJL, 947, L30
Ceau, A., Mary, D., Greenbaum, A., et al. 2019, A&A, 630, A120
Cushing, M. C., Kirkpatrick, J. D., Gelino, C. R., et al. 2011, ApJ, 743, 50
Cushing, M. C., Schneider, A. C., Kirkpatrick, J. D., et al. 2021, ApJ, 920, 20
De Furio, M., Lew, B., Beichman, C., et al. 2023, ApJ, 948, 92
Fontanive, C., Bedin, L. R., De Furio, M., et al. 2023, MNRAS, 526, 1783
Gagné, J., Mamajek, E. E., Malo, L., et al. 2018, ApJ, 856, 23
Griffith, R. L., Kirkpatrick, J. D., Eisenhardt, P. R. M., et al. 2012, AJ, 144, 148
Kammerer, J., Cooper, R. A., Vandal, T., et al. 2023, PASP, 135, 014502
Karalidi, T., Marley, M., Fortney, J. J., et al. 2021, ApJ, 923, 269
Kirkpatrick, J. D., Cushing, M. C., Gelino, C. R., et al. 2013, ApJ, 776, 128
Kirkpatrick, J. D., Gelino, C. R., Cushing, M. C., et al. 2012, ApJ, 753, 156
Kirkpatrick, J. D., Martin, E. C., Smart, R. L., et al. 2019, ApJS, 240, 19

Kirkpatrick, J. D., Gelino, C. R., Faherty, J. K., et al. 2021, ApJS, 253, 7
Kirkpatrick, J. D., Marocco, F., Gelino, C. R., et al. 2024, ApJS, 271, 55
Kühnle, H., Patapis, P., Mollière, P., et al. 2024, arXiv: 2410.10933
Lacy, B., & Burrows, A. 2023, ApJ, 950, 8
Leggett, S. K., & Tremblin, P. 2023, ApJ, 959, 86
Leggett, S. K., & Tremblin, P. 2024, RNAAS, 8, 13
Leggett, S. K., & Tremblin, P. 2025, ApJ, 979, 145
Leggett, S. K., Tremblin, P., Esplin, T. L., Luhman, K. L., & Morley, C. V. 2017, ApJ, 842, 118
Leggett, S. K., Tremblin, P., Phillips, M. W., et al. 2021, ApJ, 918, 11
Lew, B. W. P., Roellig, T., Batalha, N. E., et al. 2024, AJ, 167, 237
Lucas, P. W., Tinney, C. G., Burningham, B., et al. 2010, MNRAS, 408, L56
Luhman, K. L. 2014, ApJL, 786, L18
Luhman, K. L., Tremblin, P., Alves de Oliveira, C., et al. 2024, AJ, 167, 5
Marley, M. S., Saumon, D., Visscher, C., et al. 2021, ApJ, 920, 85
Marocco, F., Kirkpatrick, J. D., Meisner, A. M., et al. 2020, ApJL, 888, L19
Marocco, F., Eisenhardt, P. R. M., Fowler, J. W., et al. 2021, ApJS, 253, 8
Martinache, F. 2010, ApJ, 724, 464
Meisner, A. M., Leggett, S. K., Logsdon, S. E., et al. 2023, AJ, 166, 57
Meisner, A. M., Caselden, D., Kirkpatrick, J. D., et al. 2020, ApJ, 889, 74
Morley, C. V., Marley, M. S., Fortney, J. J., et al. 2014, ApJ, 787, 78
Morley, C. V., Mukherjee, S., Marley, M. S., et al. 2024, ApJ, 975, 59
Mukherjee, S., Fortney, J. J., Morley, C. V., et al. 2024, ApJ, 963, 73
Phillips, M. W., Tremblin, P., Baraffe, I., et al. 2020, A&A, 637, A38
Pinfield, D. J., Gromadzki, M., Leggett, S. K., et al. 2014, MNRAS, 444, 1931
Rieke, M. J., Kelly, D. M., Misselt, K., et al. 2023, PASP, 135, 028001
Schneider, A. C., Cushing, M. C., Kirkpatrick, J. D., et al. 2015, ApJ, 804, 92
Showman, A. P., Tan, X., & Zhang, X. 2019, ApJ, 883, 4
Suárez, G., & Metchev, S. 2023, MNRAS, 523, 4739
Suárez, G., Vos, J. M., Metchev, S., Faherty, J. K., & Cruz, K. 2023, ApJL, 954, L6
Tinney, C. G., Faherty, J. K., Kirkpatrick, J. D., et al. 2014, ApJ, 796, 39
Tu, Z., Wang, S., & Liu, J. 2024, ApJ, 976, 82
Vos, J. M., Allers, K. N., & Biller, B. A. 2017, ApJ, 842, 78
Zahnle, K. J., & Marley, M. S. 2014, ApJ, 797, 41
Zuckerman, B. 2018, ApJ, 870, 27